JACS
JOURNAL OF THE AMERICAN CHEMICAL SOCIETY

Article

pubs.acs.org/JACS

Polyprodrug Amphiphiles: Hierarchical Assemblies for Shape-Regulated Cellular Internalization, Trafficking, and Drug Delivery

Xianglong Hu,[†] Jinming Hu,*[,†] Jie Tian,[‡] Zhishen Ge,[†] Guoying Zhang,[†] Kaifu Luo,[†] and Shiyong Liu*[,†]

[†]CAS Key Laboratory of Soft Matter Chemistry, Hefei National Laboratory for Physical Sciences at the Microscale, Department of Polymer Science and Engineering, University of Science and Technology of China, Hefei, Anhui 230026, China

[‡]Engineering and Materials Science Experiment Center, University of Science and Technology of China, Hefei, Anhui 230027, China

Supporting Information

ABSTRACT: Solution self-assembly of block copolymers (BCPs) typically generates spheres, rods, and vesicles. The reproducible bottom-up fabrication of stable planar nanostructures remains elusive due to their tendency to bend into closed bilayers. This morphological vacancy renders the study of shape effects on BCP nanocarrier-cell interactions incomplete. Furthermore, the fabrication of single BCP assemblies with built-in drug delivery functions and geometry-optimized performance remains a major challenge. We demonstrate that PEG-*b*-PCPTM polyprodrug amphiphiles, where PEG is poly(ethylene glycol) and PCPTM is polymerized block of reduction-cleavable camptothecin (CPT) prodrug monomer, with >50 wt % CPT loading content can self-assemble into four types of uniform nanostructures including spheres, large compound vesicles, smooth disks, and unprecedented staggered lamellae with spiked periphery. Staggered lamellae outperform the other three nanostructure types, exhibiting extended blood circulation duration, the fastest cellular uptake, and unique internalization pathways. We also explore shape-modulated CPT release kinetics, nanostructure degradation, and in vitro cytotoxicities. The controlled hierarchical organization of polyprodrug amphiphiles and shape-tunable biological performance opens up new horizons for exploring next-generation BCP-based drug delivery systems with improved efficacy.

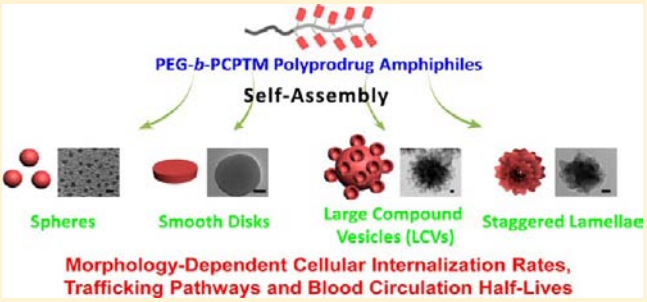

INTRODUCTION

Learning from the hierarchical structures and functions of complex biological systems such as viral capsids, discoidal red blood cells (RBCs), and platelates, has greatly promoted the biomimetic engineering of synthetic materials.[1−7] In the biomedical field, synthetic nanostructures are routinely utilized as nanocarriers for the delivery of therapeutic drugs and imaging agents. Their fabrication mainly involves top-down and bottom-up approaches.[8] For the former, particle replication in nonwetting templates (PRINT) technology developed by DeSimone[9−12] and film-stretching technique proposed by Mitragotri[13−15] represent two most recent advances. Both of them allow for highly controlled fabrication of uniform micro- and nanoparticles (NPs) with controlled shapes; however, there are limitations such as huge investment in apparatus, complicated fabrication procedures, and considerable technical challenges for the fabrication of <100 nm NPs. As opposed to top-down approaches, bottom-up ones have been more actively explored to construct hierarchically ordered nanostructures with unmatched intricacy, leading to huge success in drug and gene delivery. Among them, lipid vesicles (liposomes) and polymeric NPs (vesicles and micelles), both spherical in shape, are the two most representative types.[16−18]

Recently, scientists have been aware that NP shapes or geometries also exert important roles in determining phagocytosis, cellular interactions, and biodistribution of nanocarriers.[19−21] For example, by using particles fabricated via a film-stretching technique,[22] it was demonstrated that particle shape, instead of size, dominates the phagocytosis process. Longer blood circulation duration and specific biodistribution were observed for top-down fabricated disks compared to those of spheres.[23−25] In addition, cellular internalization of rodlike NPs, fabricated via the PRINT technique, with higher aspect ratios occurs much faster than that of lower ones.[26] However, it was also shown that spherical Au NPs exhibit much faster cellular internalization compared to Au nanorods[27] and that carbon nanotubes enter cells via unique tip-recognition and rotation mechanisms.[28] These results suggest a necessity to more carefully scrutinize the respective contribution of particle geometries, chemical compositions, and fabrication procedures toward relevant biological functions.

In the context of biomimetic fabrication of synthetic nanostructures, the bottom-up hierarchical self-assembly approach is more promising in emulating nature's sophistication.[29] For instance, solution self-assembly of block copolymers (BCPs) can lead to a variety of complex nanostructures including spheres, cylinders, lamellae, vesicles

Received: September 20, 2013
Published: October 25, 2013

ACS Publications © 2013 American Chemical Society

dx.doi.org/10.1021/ja409686x | J. Am. Chem. Soc. 2013, 135, 17617−17629

Scheme 1. Multiple Hierarchical Assemblies of PEG-*b*-PCPTM Polyprodrug Amphiphiles for Intracellular Reduction-Responsive Drug Delivery[a]

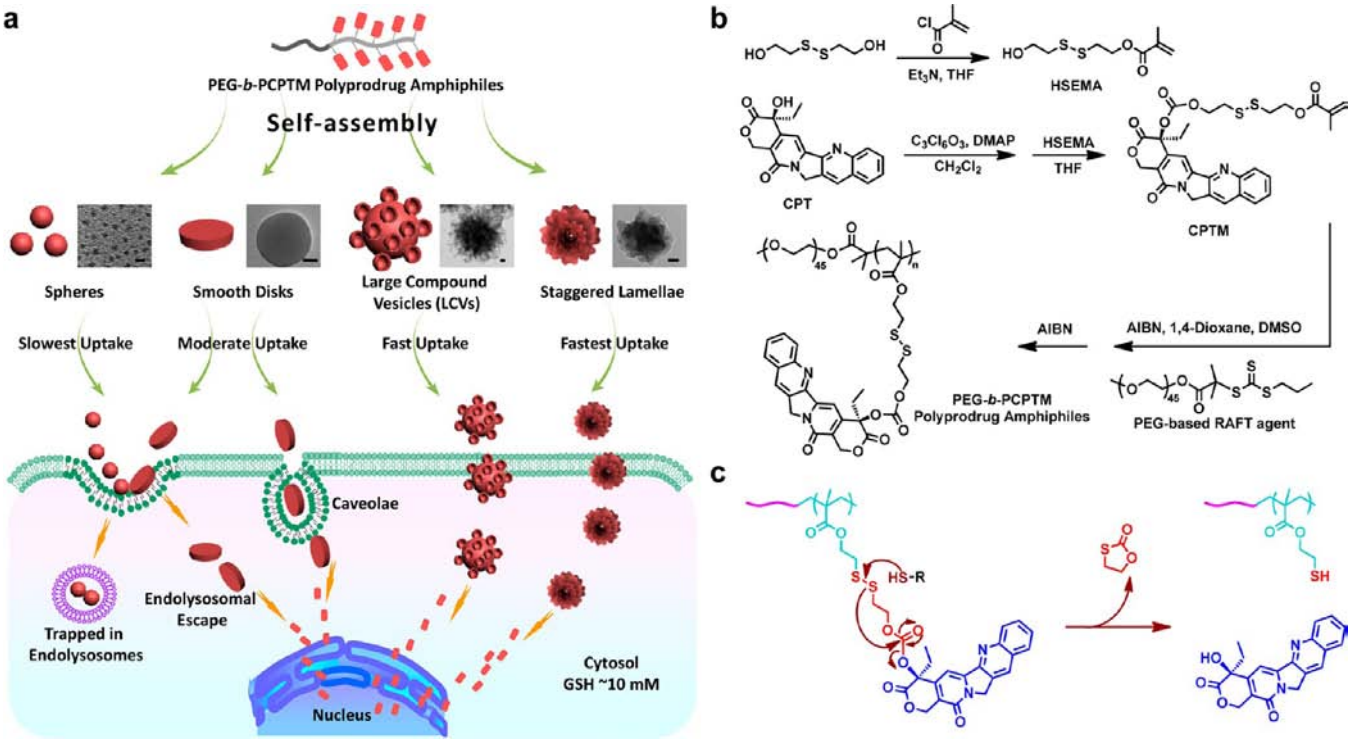

[a](a) Schematic illustration for the self-assembly of polyprodrug amphiphiles into four types of uniform nanostructures (including spheres, smooth disks, flowerlike large compound vesicles, and staggered lamellae with spiked periphery), which exhibit shape-dependent performance in the context of blood circulation, cellular internalization and transport, subcellular distribution, and degradation kinetics. (b) Synthesis of reduction-responsive CPT prodrug monomer, CPTM, and polyprodrug amphiphiles, PEG-*b*-PCPTM. (c) Proposed mechanism of reduction-responsive CPT parent drug release from PEG-*b*-PCPTM polyprodrug amphiphiles.

and bicontinuous ones, and NP geometries might also affect various biological processes.[30−32] It was previously shown that spherical BCP micelles exhibit distinct intracellular organelle distributions.[33] Self-assembled BCP filaments with longitudinal lengths reaching cellular diameters exhibited longer blood circulation times than spherical particles.[34] In addition, shell cross-linked spherical micelles self-assembled from BCPs were internalized to a greater extent than the cylindrical counterparts,[35] which is as opposed to those reported for PRINT particles of comparable geometries.[26] However, a systematic investigation and comparison of the effects of various self-assembled BCP NP shapes on cellular interactions and endocytosis is still lacking. A prerequisite for this is the controlled creation of BCP nanostructures with more complex geometries and compositions.[36−40]

Although spherical and cylindrical micelles and vesicles can be routinely fabricated via solution assembly of amphiphilic BCP in aqueous media, the reliable and reproducible fabrication of lamellae nanostructures has remained elusive.[41−44] This is mainly due to their strong tendency, being thermodynamically unfavorable, to close into vesicles to compensate for the high rim energy of open lamellae.[30,45] This morphological vacancy renders incompletion of the study of BCP nanoparticle shape effects on cellular interactions and other biological processes. In principle, the fabrication of open lamellae nanostructures can be made more feasible by introducing nonspecific interactions within hydrophobic segments to increase membrane rigidity and the corresponding curvature energy penalty.

In addition, conventional nanocarriers based on BCP assemblies are pharmaceutically inactive by themselves and only simply serve as a scaffold or physical reservoir for drugs, exhibiting intrinsic limitations such as low drug loading content, burst release and non-sustained release, and poor shelf stability.[17,46] On the other hand, drug-conjugated BCPs can endow self-assembled nanostructures with enhanced stability, but often with limitations such as low drug loading content and undesirable drug cleavage pathways. The controlled and sustained release of conjugated drugs in the active form in response to biological milieu is highly desirable.[46−49]

Thus, the fabrication of single BCP solution assemblies with built-in drug delivery functions and geometry-optimized performance remains a major challenge. Here we describe the synthesis, hierarchical self-assembly, and relevant biological functions of amphiphilic block copolymers, PEG-*b*-PCPTM, consisting of hydrophilic poly(ethylene glycol) (PEG) and polymerized block of reduction-responsive camptothecin (CPT) prodrug monomer (Scheme 1). These diblock copolymers are termed as *polyprodrug amphiphiles*, with considerably high drug loading content (>50 wt %). They can self-assemble into four types of uniform and stable nanostructures including spheres, flowerlike large compound vesicles (LCVs), and in particular smooth disks and staggered lamellae with spiked periphery, with the latter being unprecedented. Among these, staggered lamellae outperform the rest of the three NP types, exhibiting extended blood circulation duration, the fastest cellular uptake, and unique internalization pathways. We also explore reductive milieu-

dx.doi.org/10.1021/ja409686x | J. Am. Chem. Soc. 2013, 135, 17617−17629

triggered release kinetics of parent CPT drugs and nanostructure degradation, and shape-modulated *in vitro* cytotoxicities. The modularity of hierarchical self-assembly of polyprodrug amphiphiles and BCP nanostructure geometry-correlated biological functions exhibited in this system is a significant advance toward the design of next-generation drug conjugates and nanocarriers.

RESULTS AND DISCUSSION

Synthesis of PEG-*b*-PCPTM Polyprodrug Amphiphiles. We choose CPT, which is isolated from Chinese *Camptotheca acuminata* (happy tree), as the model drug due to its remarkable anticancer activity and that the *20*-hydroxyl functionality remains to be functionalizable, but with poor solubility and stability in aqueous media. The hydrophobic prodrug monomer, CPTM, was synthesized via two-step procedures in an overall yield of >60% (Scheme 1b). ^{1}H NMR, ^{13}C NMR, APCI-MS, and RP-HPLC analyses of CPTM confirmed its chemical structure (Figure S1 in the Supporting Information [SI]). The concept of conjugating small molecular drugs onto polymer scaffolds via reversible linkers has been broadly employed,[50,51] but only a few examples exist for the direct polymerization of cleavable prodrug monomers.[52−56]

Here we employed reversible addition−fragmentation transfer (RAFT) technique to polymerize prodrug monomer using PEG-based macroRAFT agent, affording PEG-*b*-PCPTM amphiphilic BCPs with CPT moieties in the hydrophobic block. These *polyprodrug amphiphiles* typically possess >50 wt % drug loading content (Table 1). A series of polyprodrug amphiphiles with varying DPs of CPTM block, PEG_{45}-*b*-$PCPTM_{24}$, PEG_{45}-*b*-$PCPTM_{52}$, PEG_{45}-*b*-$PCPTM_{87}$, and dye-labeled PEG_{45}-*b*-$P(CPTM_{0.99}$-*co*-$NBD_{0.01})_{33}$, where NBD is the fluorescent dye-containing monomer, 4-(2-methylacryloyloxyethylamino)-7-nitro-2,1,3-benzoxadiazole, were synthesized with narrow molecular weight distributions and high monomer conversions (>96%) (Figure S2 in SI and Table 1). It can be envisaged that the covalently conjugated nature of CPT drug within *polyprodrug amphiphiles* will afford high loading stability, but still with capability of self-assembling in aqueous media and releasing active CPT moieties in response to intracellular reductive milieu (Scheme 1c).

Table 1. Molecular Weights, Molecular Weight Distributions, and Drug Loading Content of PEG-*b*-PCPTM Polyprodrug Amphiphiles

polyprodrug diblock amphiphiles	DP[a]	$M_{n,\,NMR}$ (kDa)[a]	$M_{n,\,GPC}$ (kDa)[b]	M_w/M_n[b]	DLC/ %[c]
PEG_{45}-*b*-$PCPTM_{24}$	24	16.6	15.9	1.19	50.3
PEG_{45}-*b*-$PCPTM_{52}$	52	33.3	32.6	1.23	54.4
PEG_{45}-*b*-$PCPTM_{87}$	87	54.2	50.3	1.21	55.9
PEG_{45}-*b*-$P(CPTM_{0.99}$-*co*-$NBD_{0.01})_{33}$	33	21.9	21.6	1.18	52.3

[a]Number averaged molecular weights of diblock copolymers and average degrees of polymerization (DPs) for the PCPTM block were determined by ^{1}H NMR. [b]Molecular weights and molecular weight distributions, M_w/M_n, were evaluated by DMF GPC with polystyrene standards. [c]Drug loading content (DLC) was calculated as the ratio of conjugated drug weight to the weight of polyprodrug amphiphiles.

Fabrication of Multiple Hierarchical Nanostructures from Polyprodrug Amphiphiles. The self-assembly process was triggered by adding water into a solution of PEG-*b*-PCPTM in organic solvents, thereby reducing the solubility of PCPTM blocks. Intriguingly, when the self-assembly was conducted at constant initial polymer concentration and also amount of organic solvents and added water, it was found that self-assembled nanostructures were strongly dependent on water addition rates and organic solvent compositions. Multiple hierarchical assemblies, including smooth disks (Figure 1a), staggered lamellae with spiked periphery (Figure 1h), flowerlike LCVs (Figure 1m) and spheres (Figure 1n), were fabricated from PEG_{45}-*b*-$PCPTM_{52}$ in a highly controlled manner. All four of these main types of nanostructures were investigated in parallel in subsequent sections. Macroscopic images of their dispersions at equal concentrations also exhibited distinct contrast (insets in Figure S3a, SI).

Using DMSO as the common solvent at 8 mL/h water addition rate, smooth disks with uniform surface electron densities were obtained from PEG_{45}-*b*-$PCPTM_{52}$ (Figure 1a−c). The average diameter of smooth disks was ∼180 nm with low size polydispersity. To further verify the disk morphology and gauge the thickness of smooth disks, the sample stage was tilted. If disks are present, the tilting process should alter the two-dimensional projections, transforming them from circles to ellipses. Indeed, the tilting image was slightly elliptical compared to the original one (Figure 1, b vs a). Meanwhile, we can clearly discern the two layered disk morphology with an overall disk thickness of ∼28.6 nm calculated from the tilting shadow (Figure 1b and Table 2). The contour length of hydrophobic PCPTM block is ∼13.1 nm, whereas the single bilayer thickness in smooth disks is ∼14.3 nm, suggesting that PCPTM segments are not fully stretched and arranged in an interdigitated manner within each bilayer.

Section analysis of tapping mode atomic force microscopy (AFM) displayed a flat surface with an average height of ∼28.4 nm, further confirming the disklike nature (insets in Figure S3b, SI). Additionally, the form factor of disk nanostructures fits the experimental data of static laser light scattering (LLS) very well, revealing a disk diameter of ∼240 nm and a height of ∼30 nm. These results are reasonable, considering the contributions from the swelling and stretching of PEG coronas in the solution state, as compared to those measured by TEM and AFM in the dry state (Figure 1a, Table 2, Figure S3a,b in SI). Uniform disk nanostructures are quite rarely observed compared to polymeric vesicles and micelles, with existing examples mostly limited to BCPs containing fluoropolymer[57−59] or semicrystalline polyethylene segments[60] or through special processing or blending.[41,57−59] The fabrication of uniform disks from amphiphilic BCPs via direct self-assembly in aqueous media is even rare.[41−43]

Keeping the water addition rate at 8 mL/h, when the organic solvent composition was changed to 1,4-dioxane/DMSO (9/1, v/v), stacked disks with less smooth periphery were obtained with a diameter of ∼260 nm (Figure 1d−f). Using pure 1,4-dioxane as the cosolvent, staggered lamellae with spiked periphery and a diameter of ∼300 nm were obtained (Figure 1g−i). To our knowledge, this type of staggered lamellae nanostructure was unprecedented in the context of BCP self-assembly. SEM images further confirmed the stacked nature of disk nanostructures and revealed the size and shape uniformity (Figure 1f and i). As previously proposed by Eisenberg et al.,[30] the observed cosolvent composition-dependent morphologies reflect combined effects of solvent characteristics (e.g., solubility parameters and dielectric constants) and kinetic control of self-assembling pathways.

dx.doi.org/10.1021/ja409686x | J. Am. Chem. Soc. 2013, 135, 17617−17629

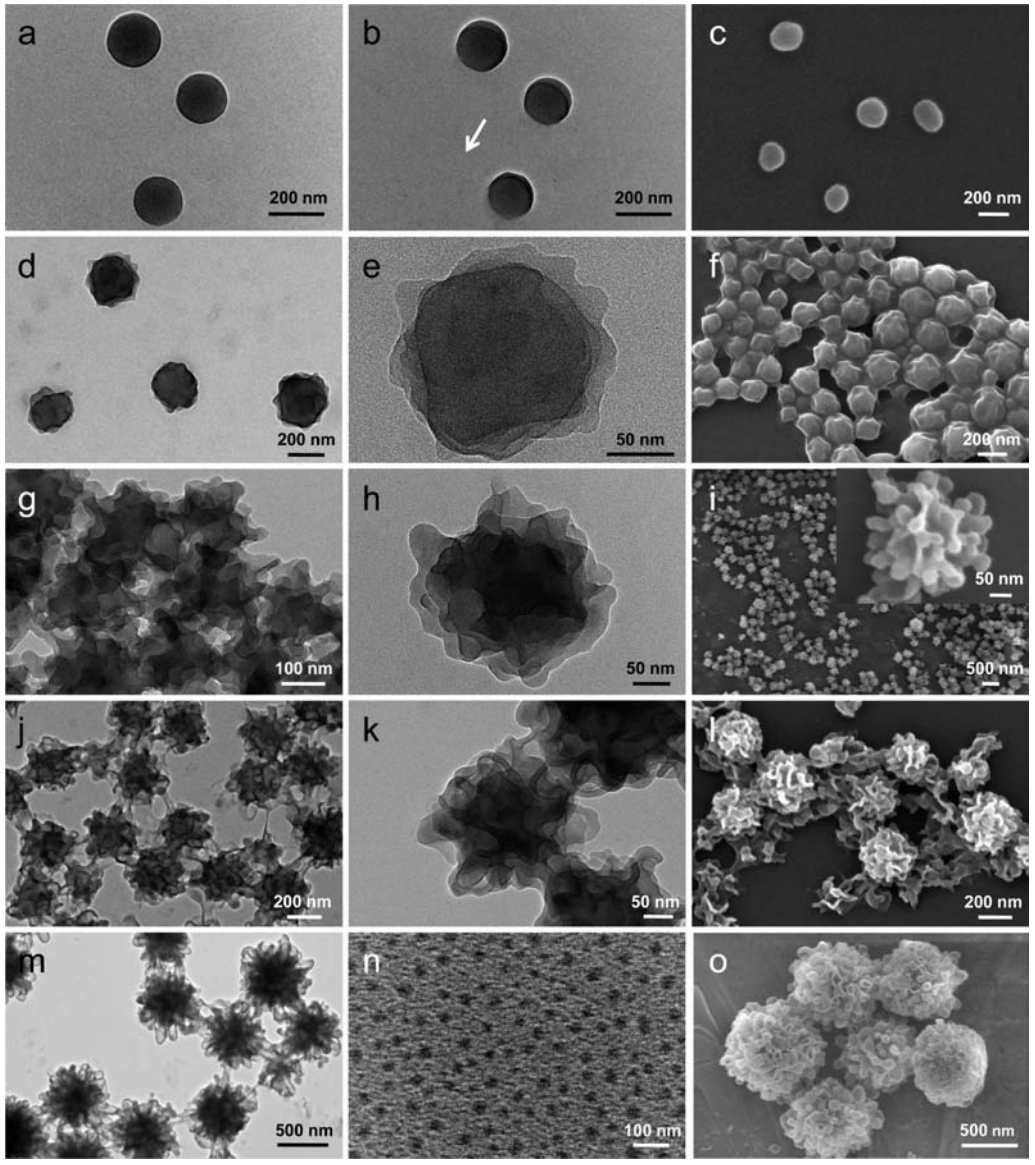

Figure 1. Multiple hierarchical assemblies fabricated from PEG_{45}-*b*-$PCPTM_{52}$ polyprodrug amphiphiles. TEM (left and middle columns) and SEM (right column) images recorded for self-assembled nanostructures formed by adding 9 mL deionized water into PEG_{45}-*b*-$PCPTM_{52}$ solution (2.0 g/L, 1 mL) in common organic solvents, in which the water addition rate and solvent composition are varied. (a–c) Disklike nanostructure with smooth periphery (pure DMSO, 8 mL/h water addition rate). (b) Image of (a) after a tilting of −20° (the arrow indicates the direction of shadowing). (d–f) Stacked disks with less smooth periphery (1,4-dioxane/DMSO (9:1, v/v), 8 mL/h water addition rate). (g–i) Staggered lamellae with spiked periphery (pure 1,4-dioxane, 8 mL/h water addition rate). (j–l) Coexistence of staggered lamellae and closed bilayers (pure 1,4-dioxane, 2 mL/h). (m and o) Flowerlike, large compound vesicles (pure 1,4-dioxane, 0.5 mL/h). (n) Spheres obtained by quickly injecting PEG_{45}-*b*-$PCPTM_{52}$ (2.0 g/L, 1 mL) solution in DMSO into 9 mL deionized water. (e, h, and k) are magnified images for (d, g, and j), respectively.

Table 2. Detailed Structural Parameters of Smooth Disks Fabricated from PEG-*b*-PCPTM Polyprodrug Amphiphiles

		LLS			diameter		thickness		
smooth disks	PCPTM length/nm[a]	$\langle R_g \rangle$/ nm[b]	$\langle R_h \rangle$/ nm[c]	ρ[d]	d_{TEM}/ nm[e]	$d_{fitting}$/ nm[f]	$h_{fitting}$/ nm[f]	$h_{tilting}$/ nm[g]	h_{AFM}/ nm[h]
PEG_{45}-*b*-$PCPTM_{24}$	6.0	71.7	78.8	0.91	109	160	20	17.8	18.6
PEG_{45}-*b*-$PCPTM_{52}$	13.1	117.8	122.7	0.96	180	240	30	28.6	28.4
PEG_{45}-*b*-$PCPTM_{87}$	21.8	85.8	92.3	0.93	153	170	60	58.3	57.3

[a]Calculated assuming a fully stretched contour length for the hydrophobic PCPTM block. [b]Average root-mean-square radius of gyration, $\langle R_g \rangle$, as determined by LLS. [c]Intensity averaged hydrodynamic radius, $\langle R_h \rangle$, as determined by LLS. [d]$\rho = \langle R_g \rangle / \langle R_h \rangle$. [e]Disk diameter as determined by TEM. [f]Disk diameter and thickness obtained by form factor fitting. [g]Thickness of smooth disks calculated by TEM tilting. [h]Thickness of smooth disks characterized by AFM section analysis.

The effect of water addition rates on the self-assembly was then explored by using pure 1,4-dioxane as the cosolvent. At a water addition rate of 2 mL/h, multigeometric NPs containing staggered lamellae and partially closed bilayer (vesicles) shapes

dx.doi.org/10.1021/ja409686x | J. Am. Chem. Soc. 2013, 135, 17617–17629

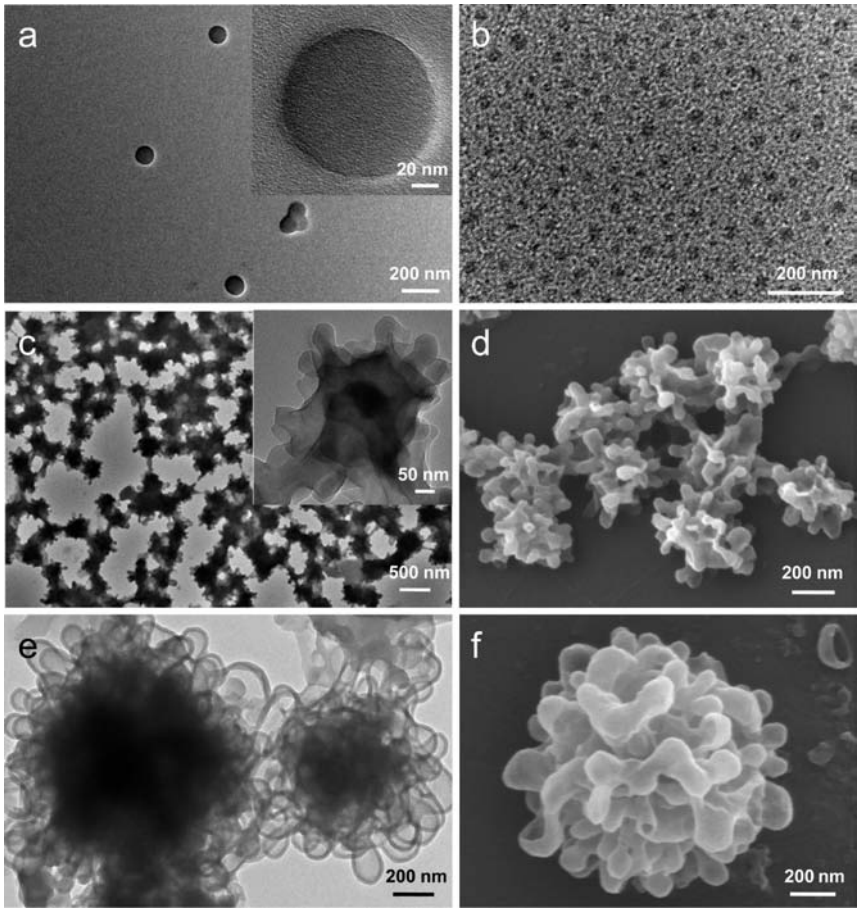

Figure 2. Four types of nanostructures self-assembled from PEG_{45}-*b*-$PCPTM_{24}$ polyprodrug amphiphiles. TEM images recorded for hierarchical assemblies fabricated from PEG_{45}-*b*-$PCPTM_{24}$ polyprodrug amphiphiles by using the same protocol as for PEG_{45}-*b*-$PCPTM_{52}$ (common solvent and water addition rate). (a) Smooth disks. (b) Spheres. (c) Staggered lamellae. (e) Flowerlike large compound vesicles. (d) and (f) are SEM images for (c) and (e), respectively (Insets: close-up shots of the corresponding nanostructures).

within the same particles with an overall diameter of ~370 nm were observed (Figure 1j–l).[40] Upon further decreasing the addition rate to 0.5 mL/h, flowerlike LCVs with a diameter of ~790 nm were obtained (Figure 1m). The corresponding SEM image demonstrated a clear three-dimensional morphology with protruding small vesicles located around the multicavity core (Figure 1o).

Finally, spherical NPs with a diameter of ~43 nm were also facilely obtained via nanoprecipitation of PEG_{45}-*b*-$PCPTM_{52}$ solution in DMSO into water (Figure 1n). Four types of typical nanostructures of PEG_{45}-*b*-$PCPTM_{52}$ all revealed monomodal hydrodynamic radius distributions as determined by dynamic LLS (Figure S3a in SI). When the self-assembly process was conducted in the presence of water-soluble calcein dye, only the LCV dispersion exhibited the strong fluorescence characteristic of calcein (Figure S3c in SI), indicating the encapsulation of hydrophilic calcein within the aqueous interior of LCVs. These results also indirectly verify the morphologies of smooth disks, staggered lamellae, and spheres, within which the encapsulation of calcein cannot be realized.

Insight into the Self-Assembling Mechanism of Polyprodrug Amphiphiles. The self-assembly of amphiphilic BCPs is typically under both thermodynamic and kinetic controls, and nanostructure morphologies can be affected by various factors such as cosolvent compositions, polymer concentrations, temperatures, and water contents and addition rates.[30] Four typical nanostructures including smooth disks, staggered lamellae, LCVs, and spheres were fabricated from PEG_{45}-*b*-$PCPTM_{52}$ BCPs by simply varying cosolvent compositions and water addition rates (Figure 1). We then attempted to explore the self-assembly mechanisms for each of these uniform nanostructures. Upon water addition at 25 °C into copolymer solution in organic solvents, the critical water contents (CWCs) defining abrupt decreases in optical transmittance were determined to be ~1 v/v%, ~5 v/v%, and ~10 v/v% during formation pathways of smooth disks (DMSO cosolvent, 8 mL/h water addition rate), LCVs (1,4-dioxane, 0.5 mL/h), and staggered lamellae (1,4-dioxane, 8 mL/h), respectively (Figure S4 in SI).

The process of smooth disk formation (DMSO, 8 mL/h water addition) was monitored at different water contents by TEM analyses (Figure S5 in SI). At 2.5 v/v% water content, primary aggregates including branching rods coexisting with possible small disks start to form. This is followed by the obvious adhesion and fusion among primary aggregates or between primary aggregates and diblock chains, leading to the formation of more disklike nanostructures at elevated water content. Further water addition leads to the freezing and retaining of disk nanostructures at ~20 v/v% water content, which qualitatively agrees with the optical transmittance results (Figure S4 in SI).

dx.doi.org/10.1021/ja409686x | J. Am. Chem. Soc. 2013, 135, 17617–17629

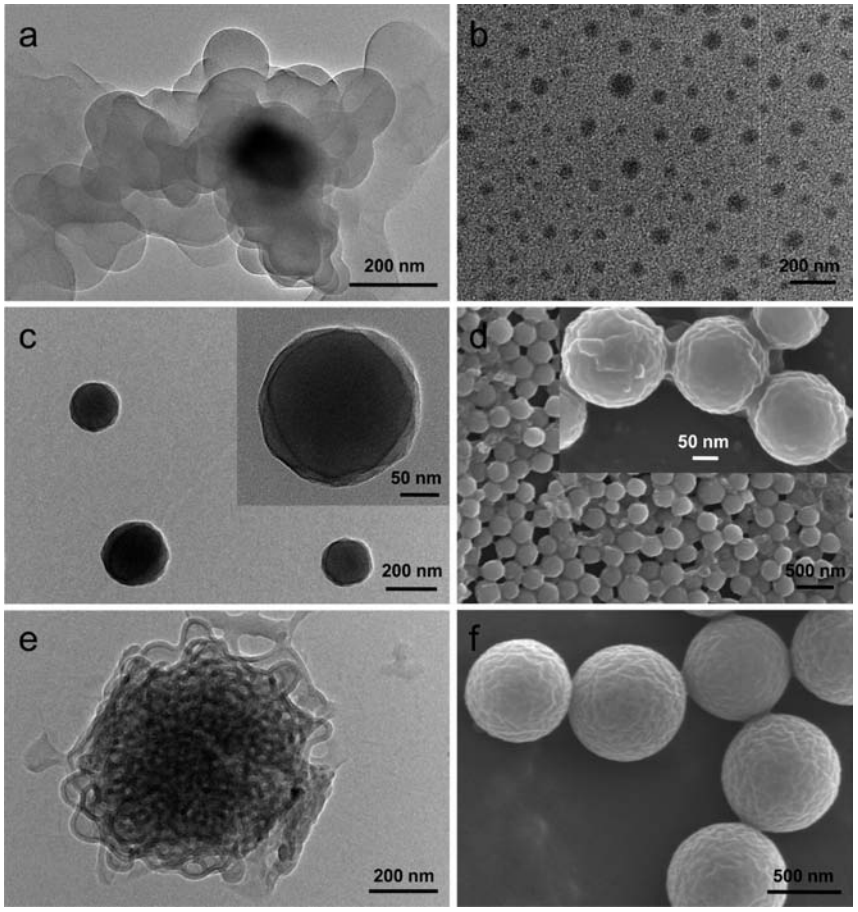

Figure 3. Multiple hierarchical assemblies of PEG_{45}-*b*-$PCPTM_{87}$ polyprodrug amphiphiles. TEM (a, b, c, e) and SEM (d, f) images recorded for nanostructures self-assembled by adding 9 mL of deionized water into PEG_{45}-*b*-$PCPTM_{87}$ solution (2.0 g/L, 1 mL) in common organic solvents, in which the water addition rate and solvent composition are varied. (a) Smooth disks (pure DMSO, 8 mL/h water addition rate). (b) Spheres obtained by quickly injecting PEG_{45}-*b*-$PCPTM_{87}$ (2.0 g/L, 1 mL) solution in DMSO into 9 mL of deionized water. (c,d) Stacked disks (pure 1,4-dioxane, 8 mL/h water addition rate). (e,f) Large compound vesicles (pure 1,4-dioxane, 0.5 mL/h water addition rate).

Employing similar fabrication procedures, smooth disks were also obtained from other polyprodrug amphiphiles with varying hydrophobic chain lengths. For example, PEG_{45}-*b*-$PCPTM_{24}$ can form smooth disks with an average diameter of ~109 nm and height of 17.8 nm (Figure 2a), and the flat disk surface with a height of ~18.6 nm was further confirmed by AFM (Figure S6c in SI insets). Polyprodrug amphiphiles with longer hydrophobic block length, PEG_{45}-*b*-$PCPTM_{87}$, can also self-assemble into smooth disks under similar conditions, exhibiting an average diameter of ~153 nm and height of ~58.3 nm (Figure 3a). For the TEM image shown in Figure 3a, individual disks appeared to irregularly aggregate to some extent, and this is probably an artifact during the preparation of TEM specimen (i.e., the drying process). Indeed, well-dispersed smooth disks of PEG_{45}-*b*-$PCPTM_{87}$ can be clearly observed when the self-assembled dispersion was further diluted to a concentration of ~0.04 g/L prior to TEM specimen preparation (Figure S7a in SI).

For nanostructures of PEG_{45}-*b*-$PCPTM_{87}$, AFM analysis revealed a flat surface with an average height of ~57.3 nm (Figure S6d in SI insets). In addition, the static LLS profiles of smooth disk dispersions of PEG_{45}-*b*-$PCPTM_{24}$ and PEG_{45}-*b*-$PCPTM_{87}$ can be well-fitted with the form factor of circular disks (Table 2, Figure S6c,d in SI). Moreover, $\langle R_g \rangle / \langle R_h \rangle$ values determined by LLS for all three smooth disk dispersions are close to 1, which match well with disk morphologies (Table 2).

To further interrogate why smooth disk nanostructures can facilely form in this system, we examined the physicochemical properties of BCPs. In DSC thermograms, CPTM monomer exhibited one endothermic melting peak at ~141.5 °C; whereas PEG_{45}-*b*-$PCPTM_{52}$ and $PCPTM_{40}$ homopolymer only exhibit glass transition temperatures, T_g, of 48.6 and 50.2 °C, respectively, and do not present any endothermic peaks (Figure S8a in SI). This demonstrates that PCPTM block in PEG_{45}-*b*-$CPTM_{52}$ does not exhibit any crystallinity, which is further confirmed by XRD analysis (Figure S8b in SI). On the other hand, upon heating BCPs film from room temperature to 180 °C, the observation under polarized optical microscopy (POM) does not reveal any textures characteristic of liquid crystal mesophases. Thus, nanostructure formation processes will not be affected by any crystallization process or liquid crystal features.

For PEG_{45}-*b*-$PCPTM_{24}$, PEG_{45}-*b*-$PCPTM_{52}$, and PEG_{45}-*b*-$PCPTM_{87}$ BCPs, the fractions of hydrophobic blocks are in the range of 34.7−65.9 mol %. Though PEG_{45}-*b*-$PCPTM_{24}$ possesses a relatively low hydrophobic fraction (34.7 mol %), it can still form stable smooth disks. However, it is expected that, for conventional uncharged BCPs with this composition, they should form spheres or rods.[61] In addition, for disklike micelles, they have a strong tendency to close up into vesicular nanostructures at the price of increased curvature energy but diminished rim energy of open lamellae. Due to the PCPTM

dx.doi.org/10.1021/ja409686x | J. Am. Chem. Soc. 2013, 135, 17617−17629

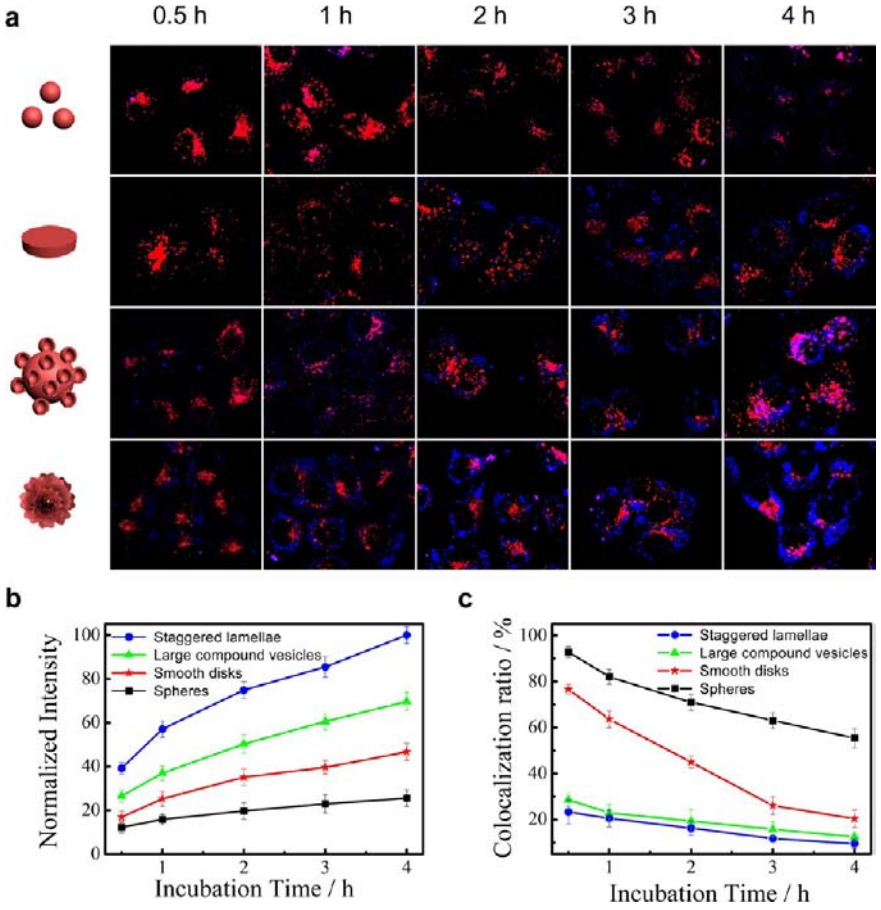

Figure 4. Cellular internalization and colocalization analysis for four types of assemblies of PEG_{45}-*b*-$PCPTM_{52}$. (a) Overlay CLSM images of HepG2 cells upon incubation with four types of distinct nanostructures (spheres, smooth disks, large compound vesicles, and staggered lamellae) with varying time intervals. The late endosomes and lysosomes were stained with Lysotracker Red (red channel), and blue channel fluorescence emission originated from CPT moieties. (b) Normalized fluorescence intensity (blue channel) of HepG2 cells was quantified from CLSM observations. (c) Colocalization ratio of blue fluorescence from polyprodrug amphiphiles with the red fluorescence of Lysotracker Red for four types of nanostructures. All data are mean values (~50 cells, three parallel experiments, $P < 0.05$).

block bearing large bulky side groups (CPT drug monomer $M_w \approx 600$ Da), we expect that the hydrophobic block will adopt a rigid chain conformation due to steric hindrance effect;[62] moreover, strong $\pi-\pi$ stacking interactions will also occur between CPT side groups. The above two factors can favorably contribute to the formation of flat membranes with relatively low interfacial curvature.[44] In addition, $\pi-\pi$ stacking interactions between PCPTM blocks within the hydrophobic membrane will accordingly elevate the curvature energy penalty during closure of rigidified membranes, thus energetically favoring open flat lamellae nanostructures instead of polymeric vesicles.

Staggered lamellae nanostructures were formed from PEG_{45}-*b*-$PCPTM_{52}$ when using 1,4-dioxane as cosolvent at a water addition rate of 8 mL/h (Figure 1g-i). The nanostructure evolution at increasing water contents was then checked. Small sheetlike primary aggregates with curled peripheries formed at 10 v/v% water content (Figure S9a in SI). Subsequent structural evolution including intense adhesion, fusion, and structural rearrangement then occurred, generating large sheetlike microstructures coexisting with discrete primary aggregates (Figure S9b–d in SI). At >40% water content, uniform staggered lamellae with irregularly spiked periphery eventually formed (Figure S9e–g in SI). Upon ultrasonication, staggered lamellae disintegrated into small sheetlike nanostructures, suggesting that they might act as primary building blocks (Figure S9a,h in SI). Tween-20 was also added into the staggered lamellae dispersion followed by extensive ultrasonication, and TEM analysis revealed uniform spherical NPs of ~23 nm in diameter, suggesting the disruption of staggered lamellae and coassembly with surfactant micelles (Figure S9i in SI). By using similar procedures, staggered lamellae with a diameter of ~380 nm were also fabricated from PEG_{45}-*b*-$PCPTM_{24}$ (Figure 2c,d). However, for PEG_{45}-*b*-$PCPTM_{87}$, stacked disks with relative smooth periphery were obtained, exhibiting an overall diameter of ~220 nm (Figure 3c,d).

The observation that water addition rates can dramatically affect self-assembling morphologies, i.e., 8 mL/h for staggered lamellae and 0.5 mL/h for LCVs, when using 1,4-dioxane as the cosolvent is actually quite serendipitous. At 0.5 mL/h water addition rate, PEG_{45}-*b*-$PCPTM_{52}$ self-assembles at first into sheetlike primary aggregates at ~5 v/v% water content (Figure S10a in SI). With progressive water addition, large aggregates were generated due to adhesion and fusion (Figure S10b–d in SI). At a water content of ~20 v/v%, only stacked lamellae morphology can be discerned, which should represent a bridging one to final formation of LCVs (Figure S10e in SI). At water contents >40 v/v%, we can observe the closure of lamellae into vesicles. Further increasing water contents leads

dx.doi.org/10.1021/ja409686x | J. Am. Chem. Soc. 2013, 135, 17617–17629

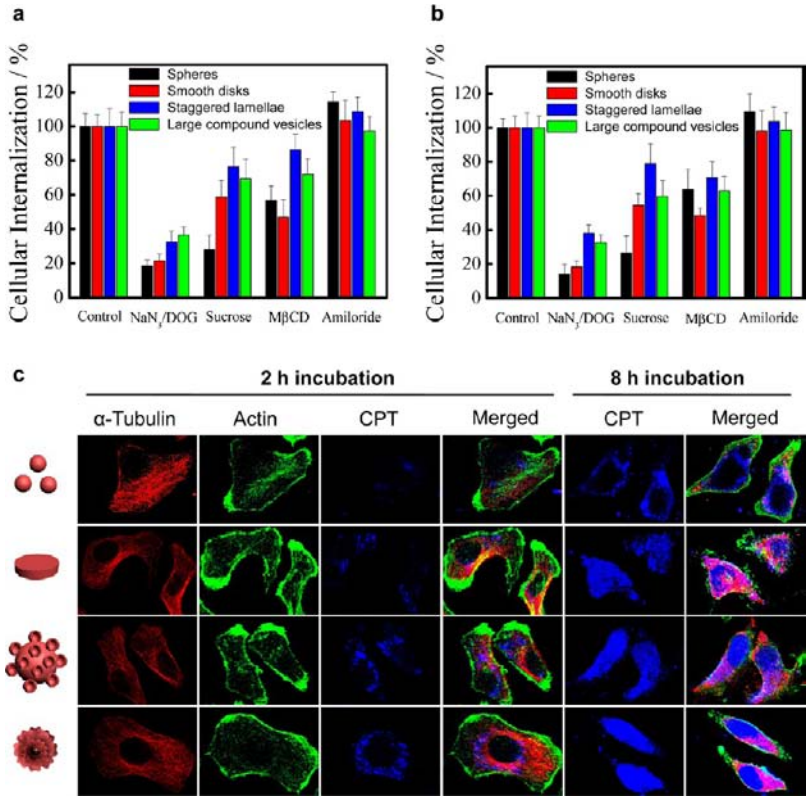

Figure 5. Probing the mechanisms of cellular internalization by using inhibitors of specific endocytic pathways and intracellular trafficking of four types of nanostructures. Cells were incubated with inhibitors indicated in the graph. (a) HepG2 cells. (b) A549 cells. Percent internalization was normalized to particle internalization in the absence of inhibitors. Data are mean values (~200 cells, three parallel experiments, $P < 0.05$). (c) CLSM images showing the intracellular distribution of CPT moieties in HepG2 cells after 2 and 8 h incubation with four types of nanostructures fabricated from PEG_{45}-*b*-$PCPTM_{52}$. Tubulin-Tracker Red (red) and Actin-Tracker Green (green) were employed to stain α-tubulin and actin, respectively.

to the maturing of LCVs and size growth of protruding small vesicles at the periphery (Figure S10f–i in SI).

The effect of water addition rates (8 mL/h vs 0.5 mL/h) on the nanostructure formation suggests that two competing processes exist: (i) decreased solvent plasticization of aggregate cores and increased bilayer rigidity and bending energy at increasing water contents; (ii) the closure of lamellae nanostructures into vesicular ones, which is a time-consuming, energy-dependent, and kinetically controlled process. If we assume 50 v/v% water content as the critical value at which all nanostructures were frozen, in the current case (1 mL diblock solution in 1,4-dioxane initially), the duration of a dynamic self-assembly process (i.e., before microstructure freezing) is estimated to be ~7 min and ~120 min at water addition rates of 8 mL/h and 0.5 mL/h, respectively. Thus, a high water addition rate favors the formation of lamellae nanostructures owing to their not being given enough time to ripen into vesicles before being kinetically frozen, whereas at a lower water addition rate, the formation of LCVs was rendered temporally possible.[63]

For polyprodrug amphiphiles with other hydrophobic chain lengths, flowerlike LCVs with a diameter of ~980 nm were also fabricated from PEG_{45}-*b*-$PCPTM_{24}$ (Figure 2e,f). In addition, LCVs of PEG_{45}-*b*-$PCPTM_{87}$ with a diameter of ~760 nm exhibit entangled and interconnected microstructures (Figure 3e). SEM image further reveals the presence of spherical aggregates with rough surfaces (Figure 3f). We speculate that these morphological differences reflect the effect of PCPTM block length variations.[64]

In addition, hydrodynamic radius distributions of four types of nanostructures of PEG_{45}-*b*-$PCPTM_{24}$ and PEG_{45}-*b*-$PCPTM_{87}$ all revealed monomodal distributions (Figure S6a,b in SI), suggesting the size and microstructure homogeneity. Furthermore, dye-labeled polyprodrug amphiphile, PEG_{45}-*b*-$P(CPTM_{0.99}$-*co*-$NBD_{0.01})_{33}$, can also self-assemble into four types of distinct nanostructures (Figure S7b–f in SI). We envisage that the observed microstructural diversities should be rooted in nonspecific interactions between hydrophobic and bulky CPT moieties within polyprodrug amphiphiles. Therefore, circular dichroism (CD) spectra were checked for aqueous dispersions of four types of nanostructures. Compared with the CD spectra of polyprodrug amphiphiles molecularly dissolved in DCM, the aqueous dispersions of their assemblies displayed enhanced signals in the CPT absorption regions at 250 nm and 300–400 nm, which well corresponded with CPT absorption peak maxima at ~250 nm and ~370 nm (Figure S11 in SI). The positive couplet signals at the highest wavelength most probably suggested the right-handed arrangement of CPT moieties within self-assembled nanostructures, implying a chiral packing of CPT moieties due to strong $\pi-\pi$ stacking interactions among CPT side functionalities, although the exact mechanism currently remains unclear and requires further exploration.[65]

Cellular Internalization and Intracellular Trafficking. The cellular internalization of four types of nanostructures, including smooth disks, staggered lamellae, LCVs, and spheres fabricated from PEG_{45}-*b*-$PCPTM_{52}$ was then examined against HepG2 cells. The kinetics of cellular uptake was evaluated by

dx.doi.org/10.1021/ja409686x | J. Am. Chem. Soc. 2013, 135, 17617–17629

quantification from CLSM analysis during the time course from 30 min to 4 h incubation (Figure 4a, Figure S12−S15 in SI). Meanwhile, late endosomes and lysosomes were stained with Lysotracker Red for colocalizing self-assembled nanostructures. It was found that the relative uptake rates were quite different for each nanostructure type (Figure 4b), with staggered lamellae exhibiting the fastest internalization rate among the four types of nanostructures. Flowerlike LCVs were internalized to a lesser extent compared to staggered lamellae, but faster than smooth disks and spheres. Slightly delayed endocytosis of spheres vs smooth disks was observed, which was consistent with previous observations by Mitragotri and co-workers[66] that cellular internalization of trastuzumab-coated disks occurred at a faster rate than that of trastuzumab-coated spheres. The relative cellular uptake rates were further confirmed by evaluating four types of nanostructures of NBD-labeled PEG-*b*-P(CPTM-*co*-NBD) using flow cytometry (Figure S16 in SI).

NP shape, size, and surface functionalities will all affect their interactions with cell membranes and consequently cellular uptake. It has been previously proposed that surface roughness of NPs can significantly accelerate their cellular internalization.[67−70] The simulation of NPs interacting with synthetic membranes demonstrates that nanoscale surface roughness can greatly minimize repulsive interactions (including electrostatic and hydrophilic repulsion), thereby promoting adhesion and entry into cells.[71,72] Thus, it is plausible to observe the relative high internalization rate of self-assembled staggered lamellae and LCVs, as compared to smooth disks and spherical micelles.

Colocalization analysis of self-assembled nanostructures and endolysosomes during cellular uptake pathways revealed that particularly low colocalization ratio was observed for both staggered lamellae and LCVs throughout the observation period (Figure 4a,c). Staggered lamellae and LCVs appeared to efficiently disperse within the entire cytoplasmic region immediately after cellular entry. The low extent of colocalization with endolysosome also suggests that staggered lamellae and LCVs either possess high endosomal escape capability or mainly follow other endocytic pathways unrelated to the endolysosomal one. In contrast, smooth disks and spheres were mainly entrapped within endolysosomes during the initial incubation duration. Upon extended incubation, smooth disks could more efficiently escape from endolysosomes compared to spheres. Further colocalization staining with endolysosomes and mitochondria for HepG2 cells and A549 cells confirmed that, upon 4 h incubation, smooth disks, staggered lamellae, and LCVs were mostly localized within the cytosol, whereas spheres were mainly trapped in endolysosomes (Figure S17 in SI). The fluorescence intensities of CPT channels further validated the relative uptake rates among the four types of nanostructures.

To probe the role of specific endocytic pathways involved in the internalization of self-assembled nanostructures, HepG2 cells and A549 cells were treated with potent biochemical inhibitors of energy-dependent processes, clathrin-mediated endocytosis, caveolae-mediated endocytosis, and macropinocytosis (Figure 5a,b). NaN_3/2-deoxyglucose (NaN_3/DOG) was employed to inhibit the energy-dependent pathway, resulting in dramatic decrease in the cellular uptake rate of all four types of nanostructures (65−86% decrease compared to control). It should be noted that no complete inhibition was observed due to the presence of glucose and exogenous ATP in the serum-free media. Sucrose treatment of cells is known to perturb clathrin-mediated endocytosis, which caused dramatic decrease (∼73%) in the uptake of spheres against two cell lines, and to a lesser extent that for smooth disks. However, no remarkable decrease was discerned for LCVs and staggered lamellae. The methyl-β-cyclodextrin (MβCD)-blocking caveolae-mediated endocytosis pathway exerts a significant effect on the uptake of smooth disks for both HepG2 cells and A549 cells, exhibiting 53% and 50% decrease, respectively. Amiloride, an inhibitor of pinocytosis, did not show any obvious effect on the endocytosis for all nanostructure types. Briefly, none of the above specific chemical inhibitors led to >90% inhibition of cellular uptake. Thus, hierarchical nanostructures of PEG-*b*-PCPM might follow multiple endocytic pathways into cells.

Among these, spherical NPs mainly follow clathrin-mediated endocytosis, whereas clathrin- and caveolae-mediated endocytosis events are both prominent pathways for smooth disks. However, clathrin- and caveolae-independent endocytosis most probably plays a crucial role for the uptake of staggered lamellae and LCVs, which bypasses the endolysosomal compartments. This is highly advantageous for the retaining of structural integrity and potency of conjugated CPT drugs within polyprodrug amphiphiles. Comparable endocytic pathways were previously proposed for the quick cellular uptake of rod NPs,[26] though remained poorly understood in the context of cell biology. It should be mentioned that the clathrin-mediated pathway is known to render the formation of primary endosomes, which consequently form late endosomes and lysosomes. Thus, spheres of PEG-*b*-PCPTM are mainly trapped within endolysosomes. These results agree well with those concluded from the colocalization analysis (Figure 4, Figure S17 in SI).

***In Vitro* Serum Stability and Degradation Kinetics of Polyprodrug Nanostructures and On-Demand Drug delivery.** Förster resonance energy transfer (FRET) technique was employed to examine the *in vitro* stability of different types of self-assembled nanostructures.[73] For nanostructures encapsulating both FRET donor and acceptor molecules (DiO and DiI) and when excited at 484 nm, energy transfer occurred and strong acceptor dye emission can be observed at ∼577 nm (Figure S18a in SI). When nanostructure dispersions were treated with 40-fold DMF (v/v), all nanostructures were disintegrated, accompanied by the prominent decrease of FRET efficiency and dramatic shift of emission peaks from ∼577 nm (acceptor emission) to ∼514 nm (donor emission). Residual nanostructure fractions (RNF%) were then quantified on the basis of changes in normalized FRET intensity ratios (see SI for details). Upon incubation for 48 h at 37 °C in pure PBS buffer, RNF values were >90% for all four types of nanostructures (Figure S18b in SI). The presence of bovine serum albumin (BSA, 45 g/L) did not exhibit obvious destruction on nanostructures after incubation for 48 h; specifically, RNF values were 83.7% for staggered lamellae, 75.6% for smooth disks, 76.9% for LCVs, and 69.6% for spheres (Figure S18c in SI). It is worthy of noting that even high content of fetal bovine serum (FBS, 90v/v%) cannot destroy these nanostructures, and RNF values were 79.1% for staggered lamellae, 74.3% for smooth disks, 68.9% for LCVs, and 59.9% for spheres (Figure S18d in SI). On the basis of the above results, staggered lamellae were found to demonstrate the highest stability among four types of self-assembled nanostructures. The observed high serum stability of nanostructures can be ascribed to strong $\pi-\pi$ stacking interactions between CPT moieties within the hydrophobic block and the protection of PEG coronas.

For nanostructures assembled from PEG-*b*-PCPTM, covalently conjugated CPT prodrug moieties are buried within

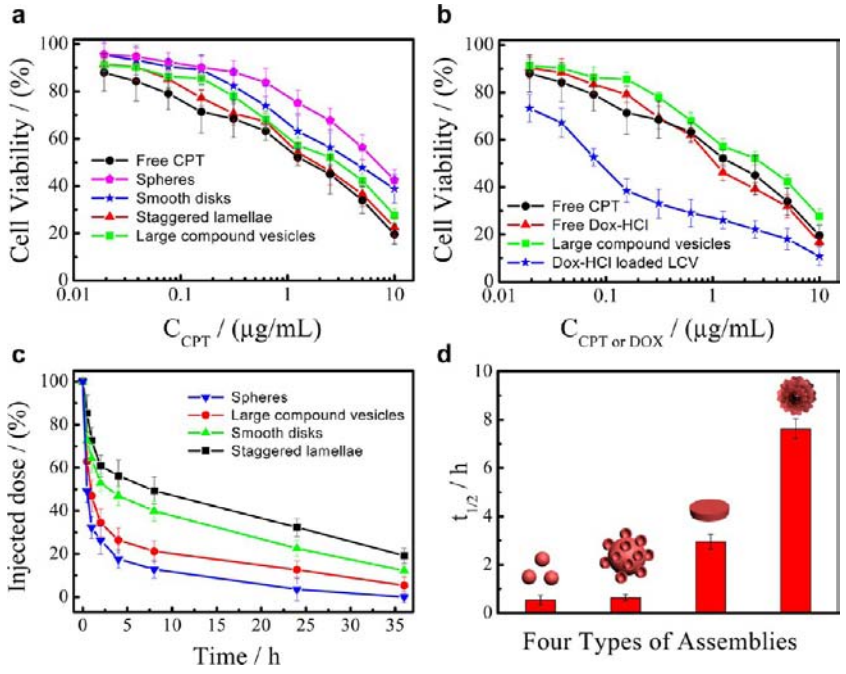

Figure 6. *In vitro* cytotoxicity and *in vivo* blood circulation studies. *In vitro* cytotoxicity determined by MTT assay against HepG2 cells upon 36 h incubation with free drug or four types of nanostructures of PEG_{45}-*b*-$PCPTM_{52}$ polyprodrug amphiphiles. (a) Free CPT, spheres, smooth disks, large compound vesicles (LCV), and staggered lamellae. (b) Free CPT, free Dox·HCl, and large compound vesicles loaded with or without Dox·HCl. (c) Time-dependent blood level upon tail vein injection of four types of nanostructures of PEG_{45}-*b*-$PCPTM_{52}$, calculated as percentage of injected dose remaining in the blood. (d) Blood circulation half-lives ($t_{1/2}$) of four types of nanostructures. Error bars were based on three rats per group at each time point and three repetitions, $P < 0.05$.

hydrophobic micellar cores or bilayer/lamellae membranes, thereby effectively preventing CPT from undesirable transformation into the inactive carboxylate form. This was confirmed by the fluorescence emission spectra (Figure S3d in SI).[74] Additionally, the CPT-containing control molecule without unsaturated double bond, CCPTM, was designed to illustrate the reduction-cleavable nature of CPTM (Figure S19a in SI). According to RP-HPLC analysis, upon treating with DTT, CPT is released from CCPTM. Comparatively, aqueous dispersion of PEG-*b*-PCPTM nanostructures upon incubation with DTT will also afford CPT parent drugs (Figure S19b in SI). Together, these results suggest that disulfide bonds in PEG-*b*-PCPTM can be cleaved under reductive milieu and the resulting thiol-containing intermediate undergoes intramolecular nucleophilic substitution at the carbonate functionality, forming a five-membered ring thiolactone and releasing CPT. These results demonstrate reduction-responsive on-demand drug release from polyprodrug amphiphiles (Scheme 1c).[55,75−77]

Dynamic LLS was employed to monitor the degradation of four types of nanostructures upon incubating with DTT to simulate tumor intracellular microenvironments (Figure S20a in SI). Spheres exhibit the fastest degradation rate, smooth disks possess slightly lower degradation rate than spheres, and staggered lamellae have the slowest degradation rate. The intermediate morphologies (6 h incubation with DTT) during degradation were then captured and observed under TEM, which agrees well with their initial morphologies and confirms prominent nanostructure disassembly (Figure S20b−e in SI). After ∼100 h incubation with DTT for staggered lamellae, no polymeric nanostructures can be observed, and the released CPT drugs just formed macroscopic sediments at the bottom of the vial (Figures S3a inset and S20f in the SI).

In vitro CPT release experiments were then performed for smooth disks, staggered lamellae and LCVs in parallel, exhibiting reduction-responsive controlled release profiles (Figure S21a−c in SI). Less than 5% cumulative CPT release was observed in the absence of DTT or in the presence of 2 μM DTT after incubating for 94 h, suggesting a minimal drug leakage during blood circulation. Upon incubation for 24 h in the presence of 10 mM DTT, high cumulative drug release was achieved in a controlled manner for the three nanostructure types; specifically, 77.3% for smooth disks, 64.5% for staggered lamellae, and 70.1% for LCVs, which corresponded well with their relative degradation rates (Figure S21a in SI). In addition, Dox·HCl release kinetics from the Dox·HCl-loaded LCVs was also performed, suggesting less than 15% cumulative release in the absence of DTT or in the presence of 2 μM DTT throughout the observation period due to limited permeability of hydrophobic vesicle bilayers,[78−80] whereas >95% cumulative release was achieved in the presence of 10 mM DTT for 24 h (Figure S21d in SI). Thus, it is possible to encapsulate other hydrophilic therapeutic drugs or inhibitors within the multi-interiors of LCVs to achieve on-demand drug co-release and combinational chemotherapy.

To further probe the fate of CPT drug moieties in cells, HepG2 cells were pretreated with four types of nanostructures for 2 and 8 h. Tubulin-Tracker Red (red) and Actin-Tracker Green (green) were employed to selectively stain α-tubulin and actin, respectively, to show cytoskeleton and cell outlines (Figure 5c). After 2 h incubation, no blue fluorescence pixels were observed for the nucleus of cells; whereas after 8 h incubation, blue fluorescence ascribing to CPT moieties uniformly dispersed in the nucleus and cytoplasm for smooth disks, staggered lamellae and LCVs, but not for spheres due to their poor endosomal escaping capability. Thus, the three

dx.doi.org/10.1021/ja409686x | J. Am. Chem. Soc. 2013, 135, 17617−17629

representative nanostructures (smooth disks, staggered lamellae, and LCVs) of polyprodrug amphiphiles can efficiently enter into the cytosol and then undergo reductive milieu-triggered cleavage, leading to the effective release of CPT in the active form and eventual accumulation within the cell nucleus.

To further probe the intracellular release of CPT drugs and differentiate the location of free CPT from polymer-conjugated CPT moieties, additional CLSM colocalization analyses among CPT moieties (blue channel), dye-labeled polymer backbones (green channel), and cell nucleus (red channel) were conducted for four types of nanostructures (Figure S7 in SI) fabricated from PEG_{45}-*b*-P($CPTM_{0.99}$-*co*-$NBD_{0.01}$)$_{33}$ (Figure S22 in SI). Upon incubation for 2 h, blue fluorescence pixels from CPT moieties generally matched well with green fluorescence pixels from NBD moieties for all types of nanostructures, except that for LCVs and staggered lamellae some blue fluorescence pixels started to separate from green ones, which might be due to their fast entry into reductive cytosol (Figure 4) and subsequent reduction milieu-triggered CPT cleavage from polymer backbones. After 8 h incubation, most blue fluorescence pixels and green fluorescence pixels separated from each other, and many blue fluorescence pixels were colocalized well with cell nucleus for smooth disks, staggered lamellae, and LCVs. For self-assembled spheres, it was hard to observe nuclear localization of CPT drugs even after 8 h incubation; in addition, the low extent of separation between blue and green fluorescence pixels further confirmed their poor endosomal escape capability (Figure 4).

***In Vitro* Cell Viability and *in Vivo* Blood Circulation of Polyprodrug Nanostructures.** *In vitro* cytotoxicity of four types of nanostructures and Dox·HCl-loaded LCVs was evaluated using MTT assay against HepG2 cells. All types of nanostructures except spheres showed cytotoxicity quite comparable with that of the CPT parent drug (Figure 6a). Additionally, Dox·HCl-loaded LCVs exhibited a higher cytotoxicity than all PEG-*b*-PCPTM nanostructures, free CPT, or Dox·HCl alone in the tested drug-equivalent concentration range (Figure 6b). This further verified the potency of combined drug delivery and intracellular co-release.

The *in vivo* blood circulation of all four types of nanostructures was studied after intravenous injection to healthy rats (Figure 6c,d). Interestingly, the elimination half-life ($t_{1/2}$) of staggered lamellae (7.62 h) was significantly higher than that of smooth disks (2.92 h), LCVs (0.64 h), and spheres (0.53 h). Thus, smooth disks and staggered lamellae possess much stealthier properties than the other two nanostructures, exhibiting a long blood circulating feature like that of RBCs due to their excellent serum stability (Figure S18 in SI) and shape resemblance but being much smaller in size than RBCs.[4,5] Persistent blood circulation is especially important in the application of therapeutic nanomedicines. Clinical results have suggested that circulation times of spherical nanocarriers are generally extended by 3-fold in humans over those in rats,[81] and so long circulation times for staggered lamellae and smooth disks in humans could also be expected. Previous reports of long blood circulation of "top-down" fabricated disk nanostructures[23−25] were again confirmed in the current system associated with "bottom-up" self-assembly. Moreover, it is surprising to find that staggered lamellae possess much stealthier blood circulation than smooth disks, which further highlights the importance of studies concerning shape and composition-modulated cellular interactions and other biological events.

CONCLUSIONS

As a novel polymeric drug delivery platform, polyprodrug amphiphiles were synthesized via controlled polymerization of stimuli-cleavable CPT prodrug monomers. PEG-*b*-PCPTM polyprodrug amphiphiles possess advantages of facile fabrication, high drug loading content (>50 wt %) and loading stability, active drug protection, blocked premature leakage, and on-demand controlled release. Multiple hierarchical nanostructures were fabricated from PEG-*b*-PCPTM polyprodrug amphiphiles with identical chemical compositions via the facile tuning of cosolvent types, compositions, and water addition rates. Four representative types of uniform nanostructures are smooth disks, unprecedented staggered lamellae, flowerlike LCVs, and spheres.

Four types of self-assembled nanostructures provide prototype models for shape-regulated cellular internalization, trafficking, and drug delivery. Staggered lamellae nanostructures displayed the fastest cellular uptake rates, with LCVs the second and spheres the slowest. Both staggered lamellae and LCVs mainly exhibit clathrin- and caveolae-independent endocytosis and bypass endolysosomal compartments during cellular transport, which differs from those exhibited by smooth disks and spheres. All nanostructure types except spheres could efficiently deliver CPT drugs into the cell nucleus, exhibiting higher cytotoxicities compared to spheres. In addition, staggered lamellae and smooth disks possess extended blood circulatory half-lives, which outperform LCVs and spheres.

The facile synthesis of *polyprodrug amphiphiles* with built-in drug delivery capability, their controlled hierarchical self-assembly, and nanostructure geometry-regulated biological functions (cellular uptake, trafficking pathways, reductive-responsive release profiles, blood circulation characteristics) well demonstrate the potency of fabricating novel nanostructures with complex chain topologies and complicated shapes for unmatched performances. The modularity of the reported nanoplatform allows for further integration with other therapeutic drugs (e.g., Dox, paclitaxel, dasatinib, dexamethasone, or therapeutic protein, DNA, and siRNA), targeting ligands, cleavable linkages, and triggering motifs, which lays a solid foundation for the invention of next-generation drug delivery systems.

ASSOCIATED CONTENT

Supporting Information

Full experimental details, NMR, APCI-MS, UV−vis, fluorescence and CD spectra, RP-HPLC, GPC, DSC, XRD, TEM, AFM and CLSM images, LLS, form factor fitting and drug release profiles. This material is available free of charge via the Internet at http://pubs.acs.org.

AUTHOR INFORMATION

Corresponding Authors

sliu@ustc.edu.cn
hjm85@mail.ustc.edu.cn

Notes

The authors declare no competing financial interest.

ACKNOWLEDGMENTS

The financial support from National Natural Scientific Foundation of China (NNSFC) Project (21274137, 21090354, 51273190, 91027026 and 51033005), Fundamental Research Funds for the Central Universities, and Specialized

Research Fund for the Doctoral Program of Higher Education (SRFDP, 20123402130010) is gratefully acknowledged.

REFERENCES

(1) Modery-Pawlowski, C. L.; Tian, L. L.; Pan, V.; McCrae, K. R.; Mitragotri, S.; Sen Gupta, A. *Biomaterials* **2013**, *34*, 526−541.
(2) Li, M.; Harbron, R. L.; Weaver, J. V. M; Binks, B. P.; Mann, S. *Nat. Chem.* **2013**, *5*, 529−536.
(3) Wilson, D. A.; Nolte, R. J. M.; van Hest, J. C. M. *Nat. Chem.* **2012**, *4*, 268−274.
(4) Merkel, T. J.; Jones, S. W.; Herlihy, K. P.; Kersey, F. R.; Shields, A. R.; Napier, M.; Luft, J. C.; Wu, H. L.; Zamboni, W. C.; Wang, A. Z.; Bear, J. E.; DeSimone, J. M. *Proc. Natl. Acad. Sci. U.S.A.* **2011**, *108*, 586−591.
(5) Doshi, N.; Zahr, A. S.; Bhaskar, S.; Lahann, J.; Mitragotri, S. *Proc. Natl. Acad. Sci. U.S.A.* **2009**, *106*, 21495−21499.
(6) Yoo, J. W.; Irvine, D. J.; Discher, D. E.; Mitragotri, S. *Nat. Rev. Drug Discovery* **2011**, *10*, 521−535.
(7) Biswas, S.; Kinbara, K.; Niwa, T.; Taguchi, H.; Ishii, N.; Watanabe, S.; Miyata, K.; Kataoka, K.; Aida, T. *Nat. Chem.* **2013**, *5*, 613−620.
(8) Venkataraman, S.; Hedrick, J. L.; Ong, Z. Y.; Yang, C.; Ee, P. L. R.; Hammond, P. T.; Yang, Y. Y. *Adv. Drug Delivery Rev.* **2011**, *63*, 1228−1246.
(9) Kelly, J. Y.; DeSimone, J. M. *J. Am. Chem. Soc.* **2008**, *130*, 5438−5439.
(10) Petros, R. A.; Ropp, P. A.; DeSimone, J. M. *J. Am. Chem. Soc.* **2008**, *130*, 5008−5009.
(11) Olson, D. A.; Gratton, S. E. A.; DeSimone, J. M.; Sheares, V. V. *J. Am. Chem. Soc.* **2006**, *128*, 13625−13633.
(12) Xu, J.; Wong, D. H. C.; Byrne, J. D.; Chen, K.; Bowerman, C.; DeSimone, J. M. *Angew. Chem., Int. Ed.* **2013**, *52*, 6580−6589.
(13) Mitragotri, S.; Lahann, J. *Nat. Mater.* **2009**, *8*, 15−23.
(14) Doshi, N.; Mitragotri, S. *Adv. Funct. Mater.* **2009**, *19*, 3843−3854.
(15) Champion, J. A.; Katare, Y. K.; Mitragotri, S. *Proc. Natl. Acad. Sci. U.S.A.* **2007**, *104*, 11901−11904.
(16) Peer, D.; Karp, J. M.; Hong, S.; Farokhzad, O. C.; Margalit, R.; Langer, R. *Nat. Nanotechnol.* **2007**, *2*, 751−760.
(17) Kataoka, K.; Harada, A.; Nagasaki, Y. *Adv. Drug Delivery Rev.* **2012**, *64*, 37−48.
(18) Matyjaszewski, K.; Tsarevsky, N. V. *Nat. Chem.* **2009**, *1*, 276−288.
(19) Tao, L.; Hu, W.; Liu, Y. L.; Huang, G.; Sumer, B. D.; Gao, J. M. *Exp. Biol. Med.* **2011**, *236*, 20−29.
(20) Wang, J.; Byrne, J. D.; Napier, M. E.; DeSimone, J. M. *Small* **2011**, *7*, 1919−1931.
(21) Champion, J. A.; Katare, Y. K.; Mitragotri, S. *J. Controlled Release* **2007**, *121*, 3−9.
(22) Champion, J. A.; Mitragotri, S. *Proc. Natl. Acad. Sci. U.S.A.* **2006**, *103*, 4930−4934.
(23) Decuzzi, P.; Godin, B.; Tanaka, T.; Lee, S. Y.; Chiappini, C.; Liu, X.; Ferrari, M. *J. Controlled Release* **2010**, *141*, 320−327.
(24) Muro, S.; Garnacho, C.; Champion, J. A.; Leferovich, J.; Gajewski, C.; Schuchman, E. H.; Mitragotri, S.; Muzykantov, V. R. *Mol. Ther.* **2008**, *16*, 1450−1458.
(25) Li, S. L.; Nickels, J.; Palmer, A. F. *Biomaterials* **2005**, *26*, 3759−3769.
(26) Gratton, S. E. A.; Ropp, P. A.; Pohlhaus, P. D.; Luft, J. C.; Madden, V. J.; Napier, M. E.; DeSimone, J. M. *Proc. Natl. Acad. Sci. U.S.A.* **2008**, *105*, 11613−11618.
(27) Chithrani, B. D.; Ghazani, A. A.; Chan, W. C. W. *Nano Lett.* **2006**, *6*, 662−668.
(28) Shi, X. H.; von dem Bussche, A.; Hurt, R. H.; Kane, A. B.; Gao, H. J. *Nat. Nanotechnol.* **2011**, *6*, 714−719.
(29) Philp, D.; Stoddart, J. F. *Angew. Chem., Int. Ed.* **1996**, *35*, 1155−1196.
(30) Mai, Y. Y.; Eisenberg, A. *Chem. Soc. Rev.* **2012**, *41*, 5969−5985.
(31) Vanhest, J. C. M.; Delnoye, D. A. P.; Baars, M. W. P. L.; Vangenderen, M. H. P.; Meijer, E. W. *Science* **1995**, *268*, 1592−1595.
(32) Zhang, L. F.; Yu, K.; Eisenberg, A. *Science* **1996**, *272*, 1777−1779.
(33) Savic, R.; Luo, L. B.; Eisenberg, A.; Maysinger, D. *Science* **2003**, *300*, 615−618.
(34) Geng, Y.; Dalhaimer, P.; Cai, S. S.; Tsai, R.; Tewari, M.; Minko, T.; Discher, D. E. *Nat. Nanotechnol.* **2007**, *2*, 249−255.
(35) Zhang, K.; Chen, Z. Y.; Germack, D. S.; Zhang, Y. M.; Fang, H. F.; Taylor, J. S. A.; Wooley, K. L. *Bioconjugate Chem.* **2008**, *19*, 1880−1887.
(36) Rupar, P. A.; Chabanne, L.; Winnik, M. A.; Manners, I. *Science* **2012**, *337*, 559−562.
(37) Gadt, T.; Ieong, N. S.; Cambridge, G.; Winnik, M. A.; Manners, I. *Nat. Mater.* **2009**, *8*, 144−150.
(38) Du, J. Z.; O'Reilly, R. K. *Chem. Soc. Rev.* **2011**, *40*, 2402−2416.
(39) Zhao, Y.; Thorkelsson, K.; Mastroianni, A. J.; Schilling, T.; Luther, J. M.; Rancatore, B. J.; Matsunaga, K.; Jinnai, H.; Wu, Y.; Poulsen, D.; Frechet, J. M. J.; Alivisatos, A. P.; Xu, T. *Nat. Mater.* **2009**, *8*, 979−985.
(40) Zhu, J.; Zhang, S.; Zhang, K.; Wang, X.; Mays, J. W.; Wooley, K. L.; Pochan, D. J. *Nat. Commun.* **2013**, *4*, 2297.
(41) Walther, A.; Drechsler, M.; Muller, A. H. E. *Soft Matter* **2009**, *5*, 385−390.
(42) Venkataraman, S.; Lee, A. L.; Maune, H. T.; Hedrick, J. L.; Prabhu, V. M.; Yang, Y. Y. *Macromolecules* **2013**, *46*, 4839−4846.
(43) Ray, J. G.; Naik, S. S.; Hoff, E. A.; Johnson, A. J.; Ly, J. T.; Easterling, C. P.; Patton, D. L.; Savin, D. A. *Macromol. Rapid Commun.* **2012**, *33*, 819−826.
(44) Song, B.; Wang, Z.; Chen, S.; Zhang, X.; Fu, Y.; Smet, M.; Dehaen, W. *Angew. Chem., Int. Ed.* **2005**, *44*, 4731−4735.
(45) Zhang, L. F.; Eisenberg, A. *Science* **1995**, *268*, 1728−1731.
(46) Ge, Z.; Liu, S. *Chem. Soc. Rev.* **2013**, *42*, 7289−7325.
(47) Hu, J. M.; Zhang, G. Q.; Liu, S. Y. *Chem. Soc. Rev.* **2012**, *41*, 5933−5949.
(48) Hu, J. M.; Liu, S. Y. *Macromolecules* **2010**, *43*, 8315−8330.
(49) Hu, J.; Zhang, G.; Ge, Z.; Liu, S. *Prog. Polym. Sci.* **2013**, DOI: 10.1016/j.progpolymsci.2013.10.006.
(50) Fox, M. E.; Szoka, F. C.; Frechet, J. M. J. *Acc. Chem. Res.* **2009**, *42*, 1141−1151.
(51) Frechet, J. M. J. *Prog. Polym. Sci.* **2005**, *30*, 844−857.
(52) Sakuma, S.; Lu, Z. R.; Kopeckova, P.; Kopecek, J. *J. Controlled Release* **2001**, *75*, 365−379.
(53) Gao, S. Q.; Lu, Z. R.; Petri, B.; Kopeckova, P.; Kopecek, J. *J. Controlled Release* **2006**, *110*, 323−331.
(54) Johnson, J. A.; Lu, Y. Y.; Burts, A. O.; Xia, Y.; Durrell, A. C.; Tirrell, D. A.; Grubbs, R. H. *Macromolecules* **2010**, *43*, 10326−10335.
(55) Parrott, M. C.; Finniss, M.; Luft, J. C.; Pandya, A.; Gullapalli, A.; Napier, M. E.; Desimone, J. M. *J. Am. Chem. Soc.* **2012**, *134*, 7978−7982.
(56) Rao, N. V.; Mane, S. R.; Kishore, A.; Das Sarma, J.; Shunmugam, R. *Biomacromolecules* **2012**, *13*, 221−230.
(57) Zhou, Z. L.; Li, Z. B.; Ren, Y.; Hillmyer, M. A.; Lodge, T. P. *J. Am. Chem. Soc.* **2003**, *125*, 10182−10183.
(58) Edmonds, W. F.; Li, Z. B.; Hillmyer, M. A.; Lodge, T. P. *Macromolecules* **2006**, *39*, 4526−4530.
(59) Lodge, T. P.; Hillmyer, M. A.; Zhou, Z. L.; Talmon, Y. *Macromolecules* **2004**, *37*, 6680−6682.
(60) Yin, L. G.; Hillmyer, M. A. *Macromolecules* **2011**, *44*, 3021−3028.
(61) Discher, B. M.; Hammer, D. A.; Bates, F. S.; Discher, D. E. *Curr. Opin. Colloid Interface Sci.* **2000**, *5*, 125−131.
(62) Bellomo, E. G.; Wyrsta, M. D.; Pakstis, L.; Pochan, D. J.; Deming, T. J. *Nat. Mater.* **2004**, *3*, 244−248.
(63) Zhang, L. F.; Eisenberg, A. *Macromolecules* **1999**, *32*, 2239−2249.
(64) Choi, S.-H.; Lodge, T. P.; Bates, F. S. *Phys. Rev. Lett.* **2010**, *104*, 047802.

(65) Cheetham, A. G.; Zhang, P. C.; Lin, Y. A.; Lock, L. L.; Cui, H. G. *J. Am. Chem. Soc.* **2013**, *135*, 2907−2910.
(66) Barua, S.; Yoo, J. W.; Kolhar, P.; Wakankar, A.; Gokarn, Y. R.; Mitragotri, S. *Proc. Natl. Acad. Sci. U.S.A.* **2013**, *110*, 3270−3275.
(67) Nel, A. E.; Madler, L.; Velegol, D.; Xia, T.; Hoek, E. M. V.; Somasundaran, P.; Klaessig, F.; Castranova, V.; Thompson, M. *Nat. Mater.* **2009**, *8*, 543−557.
(68) Verma, A.; Uzun, O.; Hu, Y. H.; Hu, Y.; Han, H. S.; Watson, N.; Chen, S. L.; Irvine, D. J.; Stellacci, F. *Nat. Mater.* **2008**, *7*, 588−595.
(69) Jewell, C. M.; Jung, J. M.; Atukorale, P. U.; Carney, R. P.; Stellacci, F.; Irvine, D. J. *Angew. Chem., Int. Ed.* **2011**, *50*, 12312−12315.
(70) Niu, Y.; Yu, M.; Hartono, S. B.; Yang, J.; Xu, H.; Zhang, H.; Zhang, J.; Zou, J.; Dexter, A.; Gu, W.; Yu, C. *Adv. Mater.* **2013**, DOI: 10.1002/adma.201302737.
(71) Hoek, E. M. V.; Agarwal, G. K. *J. Colloid Interface Sci.* **2006**, *298*, 50−58.
(72) Yang, K.; Ma, Y. Q. *Nat. Nanotechnol.* **2010**, *5*, 579−583.
(73) Lu, J.; Owen, S. C.; Shoichet, M. S. *Macromolecules* **2011**, *44*, 6002−6008.
(74) Chourpa, I.; Millot, J. M.; Sockalingum, G. D.; Riou, J. F.; Manfait, M. *Biochim. Biophys. Acta* **1998**, *1379*, 353−366.
(75) Saito, G.; Swanson, J. A.; Lee, K. D. *Adv. Drug Delivery Rev.* **2003**, *55*, 199−215.
(76) Lee, M. H.; Kim, J. Y.; Han, J. H.; Bhuniya, S.; Sessler, J. L.; Kang, C.; Kim, J. S. *J. Am. Chem. Soc.* **2012**, *134*, 12668−12674.
(77) Dunn, S. S.; Tian, S. M.; Blake, S.; Wang, J.; Galloway, A. L.; Murphy, A.; Pohlhaus, P. D.; Rolland, J. P.; Napier, M. E.; DeSimone, J. M. *J. Am. Chem. Soc.* **2012**, *134*, 7423−7430.
(78) Marguet, M.; Bonduelle, C.; Lecommandoux, S. *Chem. Soc. Rev.* **2013**, *42*, 512−529.
(79) Palivan, C. G.; Fischer-Onaca, O.; Delcea, M.; Itel, F.; Meier, W. *Chem. Soc. Rev.* **2012**, *41*, 2800−2823.
(80) Dinsmore, A. D.; Hsu, M. F.; Nikolaides, M. G.; Marquez, M.; Bausch, A. R.; Weitz, D. A. *Science* **2002**, *298*, 1006−1009.
(81) Gabizon, A.; Shmeeda, H.; Barenholz, Y. *Clin. Pharmacokinet.* **2003**, *42*, 419−436.